IR-REMPI Double Resonance Spectroscopy: The Near-IR Spectrum of NO−Ar Revisited[†]

B. Wen, Y. Kim, and H. Meyer*

Department of Physics and Astronomy, The University of Georgia, Athens, Georgia 30602-2451

J. Kłos and M. H. Alexander

Department of Chemistry and Biochemistry and Institute for Physical Sciences and Technology, University of Maryland, College Park, Maryland 20742-2021

Received: March 31, 2008; Revised Manuscript Received: May 9, 2008

We describe a new approach to IR−UV double resonance spectroscopy of NO-containing van der Waals complexes. The basic idea combines REMPI detection through a hot band transition with a simultaneous frequency scan of the IR and UV lasers in such a way that the combined photon energy is kept constant throughout the scan, matching a UV resonance transition in the system. As a result, the two-dimensional frequency problem is reduced to a fixed number of one-dimensional frequency scans, each defined by a particular photon energy sum. The method is applied to the near-IR spectrum of NO−Ar using hot band detection via the electronic A state of the complex. In the frequency range from 3718 to 3765 cm^{-1}, we recorded the previously known vibrational bands with improved frequency resolution. The increased sensitivity of the present experiment allowed us to measure for the first time their overtone, combination, and hot bands. Through the comparison with results of a close-coupling (CC) calculation, we were able to assign most of the rovibrational structures of the spectrum. Except for the first intermolecular stretch level, the band positions and rotational structures of the observed bands are in good agreement with the predictions of the CC calculations.

1. Introduction

Over the past decades, many scattering and spectroscopy experiments have been designed to study various aspects of weak intermolecular interactions.[1–3] Systems involving open-shell atoms or molecules have attracted particular interest because of the nonadiabatic aspects of the dynamics. The electronic orbital and/or spin angular momentum can couple with the orbital angular momentum of the collision partner, causing nonadiabatic effects like electronic energy transfer. Besides complexes involving hydride radicals,[4,5] NO-containing clusters have emerged as prototypical systems. In particular, the collision dynamics of the NO−Ar system has been studied extensively both experimentally as well as theoretically.[6–10]

Spectroscopic investigation of the NO−Ar complex has been reported by several groups.[11] While much work concentrated on the excited Rydberg states, Mills et al. and recently also Sumiyoshi and Endo used microwave and radio frequency spectroscopy to study rotational transitions between a number of multiplet levels associated with the lowest rotational levels of the complex.[12–14] From the analysis of these data, Sumiyoshi and Endo determined a set of two-dimensional potential energy surfaces (PES) which reproduce the experimental microwave data. The resulting PESs are very similar to the ab initio PESs reported by Alexander.[15,16] Clearly, a more sensitive test of these PESs would be the comparison of the predicted energies of the NO−Ar bound stretch and bending energy levels with experimental data.

In our laboratory, we have applied IR-REMPI double resonance spectroscopy to study the intermolecular modes of complexes containing NO. We were able to record spectra for the systems NO−Ar and NO−Ne.[17,18] In these experiments, we employed (2 + 1) REMPI (resonance-enhanced multiphoton ionization) via various Rydberg states of NO for the IR detection step. In most cases, the X → Rydberg state spectrum consists of a multitude of vibrational bands with essentially no resolved end-over-end rotational structure. Some rotational structures due to *z*-axis rotation were resolved at the resolution of the UV laser systems employed. The density of accessible rotational levels was further enhanced by the relaxed selection rules for the two-photon process. The large number of overlapping bands allowed us to use a fixed UV frequency for monitoring the IR absorption during a scan of the IR laser. Nevertheless, it was necessary to use different UV frequencies for detecting the various bands associated with different intermolecular vibrations. This implies further that the scheme does not provide a guarantee to find very weak absorption bands. If none are found, it could simply indicate that the UV frequency used is not correct. On the other hand, a full two-dimensional scan of UV and IR frequencies is not feasible for most systems.

Another drawback of our previous approach is the failure to detect REMPI spectra involving higher Rydberg states for molecular, rather than atomic, complexes of NO, for example, with N_2, CO, CO_2, CH_4, NH_3, or acetaldehyde. On the other hand, intense (1 + 1) REMPI spectra in the region of the NO A state have been reported in the literature for several of these complexes.[19–21] A disadvantage of A state detection is that the complexes of this state of NO tend to be more weakly bound than those of states correlating to higher NO Rydberg states. As a result, the spectra exhibit fewer vibrational bands. Because of the one-photon selection rules, we also expect fewer rotational lines in comparison with the two-photon case.

In this article, we report how many of the problems discussed above can be avoided through the use of either hot band or sequence band detection via the A state of NO in combination with a simultaneous frequency scan of the IR and the UV lasers

---

[†] Part of the "Stephen R. Leone Festschrift".

* To whom correspondence should be addressed.

10.1021/jp802765z CCC: $40.75

in which the combined photon energy is kept constant throughout the scan to match a UV resonance transition in the system. Such a variant of IR−UV double resonance spectroscopy has been developed previously as a spectroscopic filter to identify and distinguish bright and dark states in highly vibrationally excited acetylene.[22,23] We apply this approach to IR−UV double resonance spectroscopy to the near-IR spectrum of the NO−Ar system. Several of the bands reported previously[17,24] have been remeasured with improved sensitivity and spectral resolution. Furthermore, the simultaneous scan of both the IR and the UV lasers enabled us to measure, for the first time, various overtone, combination, and hot bands of the intermolecular vibrations.

The paper is organized as follows. A short section on the theoretical treatment is followed by an Experimental Section, in which we review briefly the original double resonance setup and describe in detail the modifications implemented recently. This section is followed by a description of the Experimental Results. In section 5, we present the Spectroscopic Analysis and Discussion followed by the Conclusions.

2. Bound-State Calculations

Fully quantum close-coupling (CC) and coupled-states (CS) calculations of bound states were performed for the Ar−NO($r = r_e$) PES of Alexander.[15,16] In these calculations, the open-shell electronic structure of the NO molecule was taken into account. We employed the HIBRIDON suite of codes.[25] In the bound-state calculations, the potential is represented in terms of the diabatic PESs V_{sum} and V_{diff}. They are defined as the half-sum and the half-difference of the adiabatic PESs corresponding to the NO−Ar electronic states of A″ and A′ reflection symmetry,[26] which are determined by the ab initio calculations.

The radial part of the wave functions in the bound-state calculations is represented by a replicated Gaussian basis[27] distributed between $R = 4.5$ and 25 bohr. As molecular parameters, we used a reduced mass of 17.135 amu for NO−Ar and a rotational constant of $B = 1.69611$ cm^{-1} for NO. For the electronic structure of NO($\nu_{\mathrm{NO}} = 0$), we took a spin−orbit constant $A_{\mathrm{so}} = 123.1393$ cm^{-1} and used the Λ-doubling parameters $p = 0.01172$ cm^{-1} and $q = 0.67$ cm^{-1}. The channel basis included all rotational levels of NO up to $j_{\max} = 12.5$, which was sufficient to converge the energies of all bound states for values of the total angular momentum ranging from $J = 1/2$ to 9/2. In the CS calculations, we retained the same parameters and performed calculations, separately, for each allowed value of the body-frame projection quantum number P of $\vec{J}$.

Our analysis of the near-IR cluster spectra will be guided by the earlier theoretical calculations by Alexander and co-workers.[15,16] Alexander showed that an adiabatic-bender model[28,29] provides an excellent approximation to the bound-state energies of the complex. We additionally impose the centrifugal-sudden (coupled-states) approximation,[30] within which the projection P of the total angular momentum vector onto the body-fixed z-axis is a good quantum number. For each value of P and J, diagonalization of the CS Hamiltonian as a function of the NO−Ar distance yields a set of adiabatic potentials. Solution of a one-dimensional Schrödinger equation gives rise to a set of vibrational energy levels for each of the “adiabatic-bender” potentials. The energies of these levels can be labeled as J, P, n (the canonical number of the corresponding adiabatic-bender potential), and ν (the vibrational quantum number within the nth adiabatic-bender potential). To a good approximation, we have found that n and v can be identified with the bending ν_b and stretching ν_s quantum numbers of the complex.

In summary, the different bound-state energies of the complex can be grouped into levels characterized by the approximate quantum numbers ν_b, ν_s, and P. Because this article focuses on the near-IR spectrum of the NO−Ar complex, it will be convenient to specify also the NO vibrational quantum number ν_{NO}. Hereafter, then, the different levels of the complex will be labeled as (ν_{NO},ν_b,ν_s,P).

3. Experimental Section

The original setup of the double resonance experiment has been described in detail previously.[17,18] Briefly, the experiments are performed in a differentially pumped molecular beam scattering apparatus.[31,32] Molecular beam pulses of 60−80 μs duration with a repetition rate of 10 Hz are generated in the source chamber with a home-built piezoelectric molecular beam valve. The pulses travel through a skimmer into the detector chamber where they are intersected with the IR beam and the UV probe beam inside of an electrode arrangement. Created ions are accelerated in an electric field and reflected off of the molecular beam axis with an electrostatic mirror toward a microchannel plate detector (MCP). In the original setup, we used a counterpropagating arrangement for the two laser beams. Because of the large size of the molecular beam machine, this resulted in a complicated and often unstable alignment.

Furthermore, we now use a different electrode setup for ion time-of-flight (TOF) analysis.[33] In an effort to improve the velocity resolution for the measurements of scattered products, we redesigned the electrode arrangement using a combination of a velocity dispersion region and an ion acceleration region. A schematic of the present setup is shown in Figure 1. This setup can be operated in either a mass spectrometer mode or a velocity dispersion mode. In the latter mode, we use two electric fields, one for velocity dispersion and the other for ion acceleration resulting, in high velocity resolution while maintaining good detection sensitivity. In the mass spectrometer mode, the first field is used as the acceleration region, while the second region is grounded, acting as drift region. The UV beam is focused between two electrodes with a lens of 300 mm focal length onto the molecular beam. The incoming IR beam intersects the UV beam at an angle of 12°. It is focused with a 500 mm lens (CaF$_2$) onto the center of a multipass arrangement using two confocal gold mirrors with a radius of curvature of 200 mm. The mirrors are displaced 200 mm from the center, refocusing the diverging beams onto the center. The IR beam enters the multipass through a 3 mm hole drilled into the center of one of the gold mirrors. The alignment is facilitated by using a red laser diode beam aligned to copropagate with the IR beam. Roughly 10−12 passes are realized with as many focal spots confined to a volume of about 4 mm radius located on the molecular beam axis. Ideally, the reflected beams all lie in a single plane which contains the molecular beam axis. Because of the smaller electrode spacings, it was necessary to modify the two electrodes adjacent to the UV beam. These electrodes now have a 7 mm wide horizontal cut on either the side facing the incoming UV beam or on the opposite side. Unfortunately, directional fluctuations in the output of the OPO can be amplified in the multipass setup, causing a fraction of the reflected IR beam to hit one of the electrodes. The resulting photoelectrons are accelerated in the electric field and, through electron impact ionization, generate large ion densities which, in turn, can cause serious baseline shifts on the ion detector. Therefore, some experiments were performed with only one mirror reflecting the IR beam onto itself.

IR radiation near 2.7 μm is generated with an optical parametric oscillator (OPO) (Continuum Mirage 3000). The

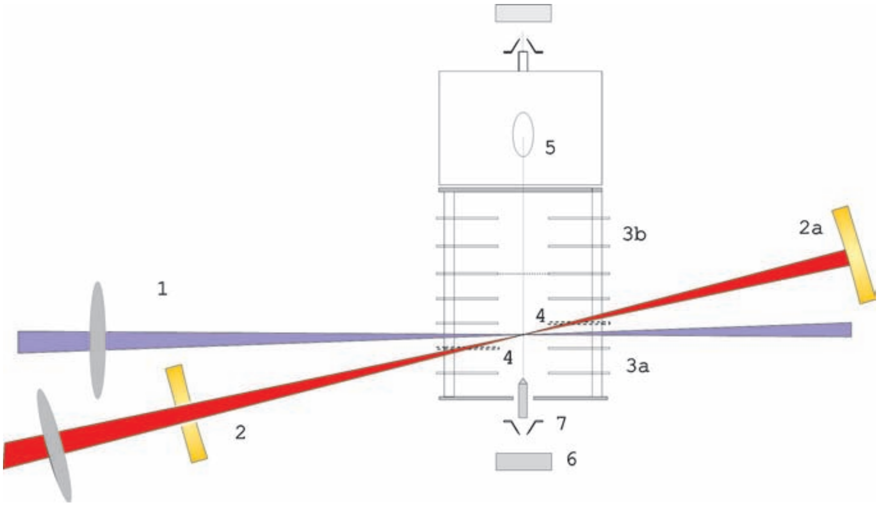

Figure 1. Schematic of the experimental setup for the IR−UV double resonance experiment; (1) UV laser, (2) IR laser, (2a) IR multipass, (3) electrode setup, (3a) velocity dispersion region, (3b) acceleration region, (4) modified electrode, (5) MCP, (6) molecular beam valves, (7) skimmer.

OPO is pumped by an injection-seeded Nd:YAG laser (Continuum Powerlite 7010). Details of its layout and operation are described in ref 34. As in our previous experiments, we monitor the fringes of an etalon (free spectral range FSR = 0.200918 cm^{-1}, finesse 12) and the photo acoustic cell spectrum of NO during a scan of the IR laser. While the etalon fringes establish the relative frequency scale for the scan, the first overtone spectrum of NO provides the absolute frequency calibration.[35] Tunable UV light in the range of 225−245 nm is generated from the output of a near-grazing incidence dye laser (LAS LDL205) pumped by the third harmonic of a Nd:YAG laser (Spectra Physics GCR170-10). With the dye laser operating on Coumarin 450, we estimate the effective line width of the doubled output at the one-photon level at 0.15 cm^{-1}. In the case of sum-frequency generation from the dye output and the residual second harmonic of the Nd:YAG laser, the effective line width is approximately 2.5 cm^{-1} (see below). We use pulse energies of about 200 μJ focused with a 300 mm lens for the detection of the NO−Ar complexes. The relative timing of the two laser beam pulses and the molecular beam is controlled by three delay generators (Stanford Research Systems DG535 and Berkeley Nucleonics Corporation BNC555), two of which are controlled by the master PC for the experiment. Using two fast photodiodes (Hamamatsu: S5973), we adjust the timing of the two laser pulses in such a way that the IR laser is fired at least 30 ns before the UV probe laser. Both lasers are linearly polarized along the molecular beam axis.

We use two different spectroscopic schemes to detect vibrationally excited NO. Both schemes involve excitation to the first electronically excited-state $A^2\Sigma$ state of NO followed by ionization: hot band excitation NO $X^2\Pi$ ($\nu_{NO}'' = 1$ and 2) → NO $A^2\Sigma$ ($\nu_{NO}' = 0$) or sequence band excitation NO $X^2\Pi$ (ν_{NO}'') → NO $A^2\Sigma$ ($\nu_{NO}' = \nu_{NO}''$). Sequence band detection of NO $X^2\Pi$ ($\nu_{NO}'' =0$, 1, and 2) requires UV light at around 221, 223.5, and 226 nm, respectively.[36] These wavelengths are easily generated through frequency doubling of the output of a dye laser in a crystal of BBO (betabarium borate 59.7°, ITI-Electrooptics).

Hot band detection of NO($\nu_{NO} = 2$), requires UV light around 245 nm. Although this cannot be accomplished by simply frequency doubling the output of the dye laser, we generate 245 nm light via sum frequency generation in a BBO crystal using the dye output at around 460 nm and the residual green light of the Nd:YAG laser. The residual green beam (10 mJ) is collimated with a telescope (−50 mm, 150 mm) and combined with the dye output in a 532 nm beam splitter (75%, 45°, S, CVI-Laser Corporation) which transmits about 80% at 460 nm. The polarization of the green beam is rotated from horizontal to vertical with a half-wave plate. Both employed nonlinear processes, i.e., second harmonic and sum frequency generation, are of the type o + o → e. In fact, both processes can be realized using the same BBO crystal (cut 59.7°). The relevant phase matching curves based on the Sellmeier coefficients of ref 37 are shown in Figure 2. We see that a BBO crystal designed for SHG in the range of 430−520 nm can also be used for sum frequency generation with the Nd:YAG second harmonic at 532 nm and the same wavelength range designated for SHG. While the former covers the UV wavelength range 215−260 nm, the latter produces UV in the range of 230−260 nm. At a first glance, the wavelength range does not seem to be extended. Considering, on the other hand, the very limited gain curves of the laser dyes used in this wavelength region, there is a distinct benefit in employing sum frequency generation. For example, with the laser dye Coumarin 450, the wavelength range of 440−465 nm can be covered and thus the UV range of 220−232 nm, while the range accessed through sum frequency generation is 241−248 nm. As a result, we can use the setup with this laser dye to detect ground and vibrationally excited NO (ν_{NO}

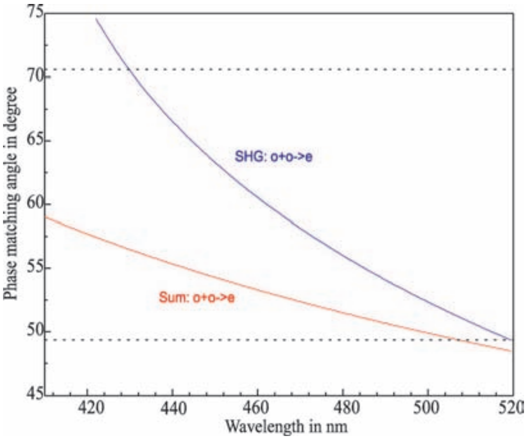

Figure 2. Collinear phase matching angle for second harmonic and sum frequency generation in BBO. The dashed curves indicate the acceptance angular range of the crystal.

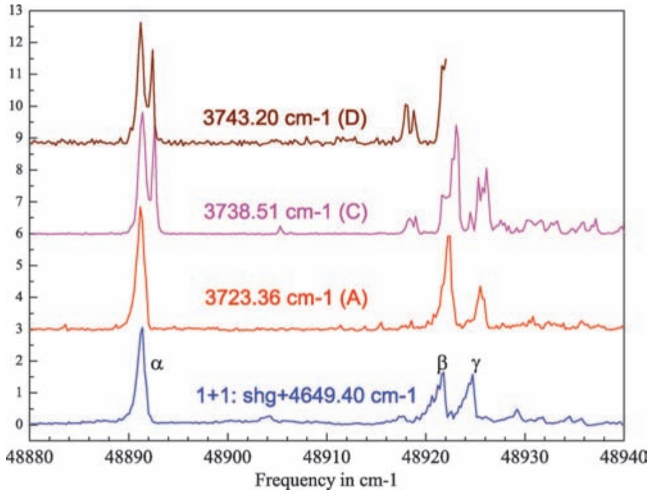

Figure 3. UV frequency scan of the 1 + 1 REMPI signal of NO(ν_{NO} = 2)−Ar with the IR frequency fixed to the indicated values. The spectra are displayed as a function of the sum of the UV frequency and the respective IR frequency. The bottom spectrum represents the pure UV 1 + 1 REMPI spectrum of NO(ν_{NO} = 0)−Ar shifted by 4649.40 cm $^{-1}$ to higher wavenumbers.

= 0,1, and 2) via sequence band excitation and NO(ν_{NO} = 2) via hot band detection. While collinear phase matching is easily realized for optimum SHG, the spatial alignment of the two laser beams used for sum frequency generation is checked by comparing the position of the two types of UV beams in the far-field. In addition, the relative spatial alignment of the UV and IR beams can be verified through IR−UV double resonance signals resulting from sequence band or hot band detection of the NO monomer.

4. Experimental Results

The most important change in the IR-REMPI double resonance experiment of NO-containing complexes is the implementation of (1 + 1) REMPI detection via the electronic A state of NO. Cluster spectra in this region are usually shifted only slightly toward the red or, occasionally, toward the blue due to the weaker interaction in the A state as compared to the more ionic interaction in the higher Rydberg states.[11] The low binding energy results in a small number of bound vibrational levels and thus in a sparse (1 + 1) REMPI spectrum. In Figure 3, we present double resonance spectra of NO−Ar for the UV region of the sequence band of NO(ν_{NO} = 2). The spectra are taken with the IR frequency fixed to transitions from the vibrationless level of NO(ν_{NO} = 0)−Ar to various intermolecular vibrations of the NO(ν_{NO} = 2)−Ar potential surface.

As we have shown in our previous work,[17] the IR spectrum of the NO−Ar complex in the region of the first overtone of NO is dominated by four bands (labeled A through D), which are assigned to the origin (Band A) and transitions to levels involving one quantum of bending (Band C) and one quantum of stretch vibration (Band D). Band B is associated with the excitation of one quantum of rotation around the z-axis, that is, P' = 1.5.[17] In Figure 3, each spectrum is displayed as a function of the sum of the UV frequency and the respective IR frequency. In this way, transitions to the same levels of the electronically excited state line up. For comparison, we also show in the lowest trace in Figure 3 the pure UV (1 + 1) REMPI spectrum of NO(ν_{NO} = 0)−Ar shifted up by 4649.4 cm^{-1}. This value corresponds to the $\nu_{NO} = 0 - \nu_{NO} = 2$ spacing in the A state of the NO monomer, apart from an additional red shift of 2.5 cm^{-1} reflecting a small change in the binding energy of the complex.

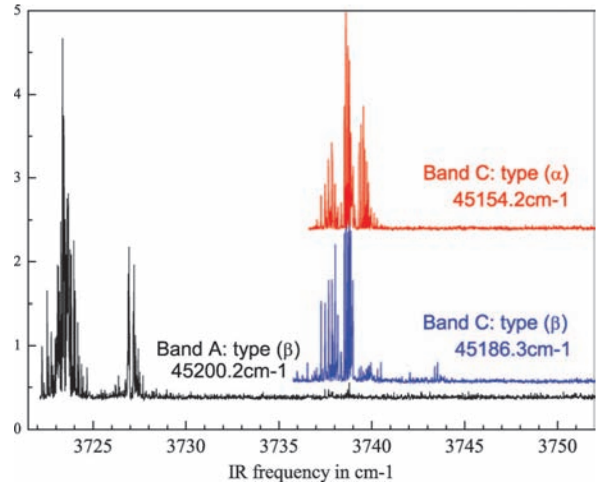

Figure 4. IR scans with fixed UV frequency (1 + 1) REMPI sequence band detection of NO(ν_{NO} = 2)−Ar at the indicated UV frequencies.

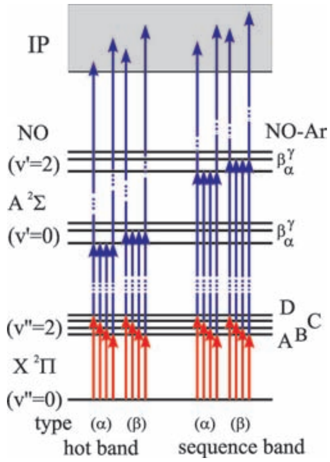

Figure 5. Double resonance schemes employing constant photon energy sum scans in combination with either hot band or sequence band detection. On the left side, we have indicated the different vibronic levels of NO, whereas the labels on the right side refer to the associated levels of the complex. IR transitions are shown in red, with the subsequent UV resonant transition and ionization step shown in blue. Different IR resonances are indicated for the scans of type (α) and type (β).

The UV spectrum is dominated by three peaks labeled α, β, and γ. These peaks are also present in the double resonance spectra. The top two double resonance spectra are taken with the IR laser fixed to the transition frequency corresponding to the excitation of one quantum of intermolecular bending or stretch vibration, respectively. While the overall structure is similar, the peaks in the top two spectra exhibit a satellite blue shifted by about 2 cm^{-1}. Most likely, this peak is due to the IR excitation of rotational levels with projection P' = 1.5 in the NO(ν_{NO} = 2)−Ar manifold.

Since other vibrational levels are not accessed with significant intensity, we conclude that a double resonance signal for NO−Ar can only be observed when one of the three A-state levels of this complex is accessed. We also notice that there is not a single UV frequency at which all major bands can be detected. This fact becomes even clearer when IR scans recorded with different UV frequencies are compared. In Figure 4, we show IR spectra with the UV frequency fixed to the indicated values. The extreme selectivity has its origin clearly in the reduced number of vibration−rotation levels in the electronically excited state.

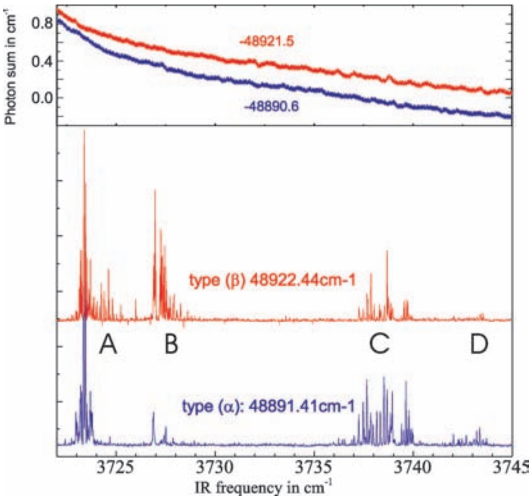

Figure 6. Constant photon energy sum scans with (1 + 1) REMPI sequence band detection of NO($\nu_{\mathrm{NO}} = 2$)−Ar type (α) and type (β). The top part shows the variation of the photon energy sum during the scan.

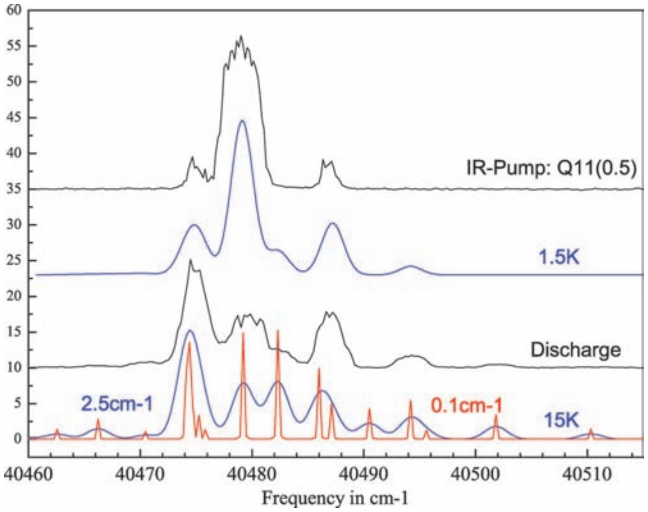

Figure 7. (1 + 1) REMPI hot band detection of NO($\nu_{\mathrm{NO}} = 2$) generated in a molecular beam discharge and through IR pumping. Calculated spectra assuming the indicated rotational temperatures and line widths are shown in color.

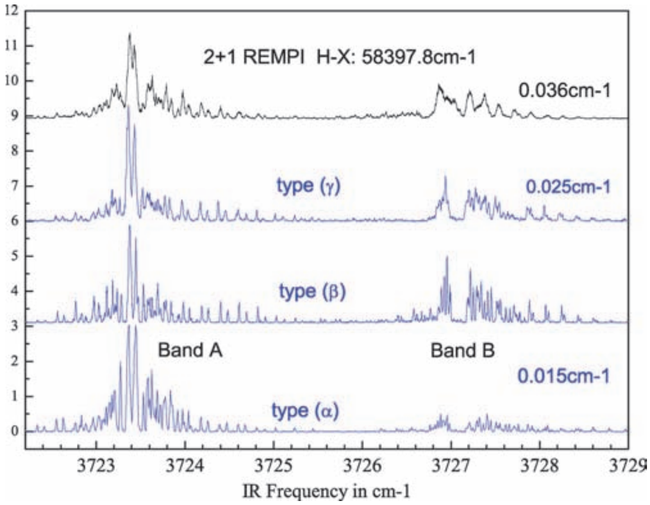

Figure 8. Comparison of bands A and B measured as constant photon energy sum scans through hot band detection of type (α), (β), and (γ). The top spectrum represents the fixed UV through (2 + 1) REMPI detection at the indicated two-photon frequency (from ref 17).

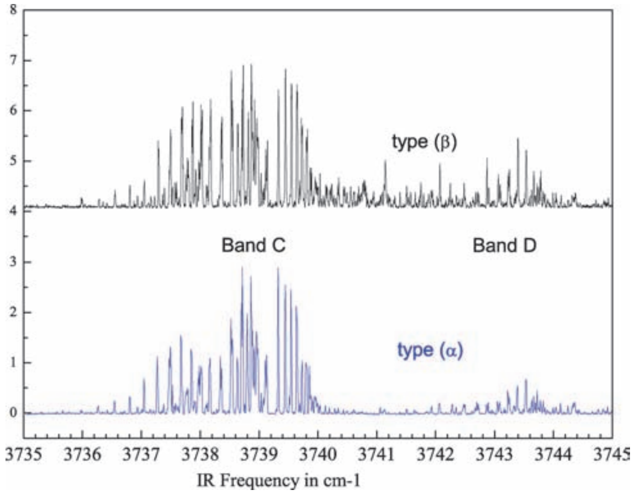

Figure 9. Comparison of constant photon energy sum scans through hot band detection types (α) and (β): bands C and D.

In the case of (2 + 1) REMPI detection of the complex, this situation is not as critical because the strongly bound Rydberg states of NO−Ar have many more levels accessible in the REMPI process. Nevertheless, even in these cases, several UV frequencies are required in order to detect the different bands. Unless a large number of UV frequencies can be tested, this approach relies on finding a signature of a new band in a previous IR scan with fixed UV frequency. In a second step, the IR frequency can be adjusted to excite the new band while the UV frequency is scanned to locate a UV frequency that is more efficient in detecting the new band. For example, the bottom trace in Figure 4, detected at 45200.2 cm^{-1}, reveals a small signal for band C, while at 45154.2 and 45186.3 cm^{-1}, band C is detected efficiently. At the latter frequency, even a small signal due to band D is revealed. Clearly, while this approach relies very much on the fortuitous recognition of small signals, it is not suitable for the detection of weak unknown bands.

These limitations are avoided by scanning simultaneously the IR and UV lasers in such a way that the sum of the photon energies is kept constant. In principle, this scheme allows the REMPI step to proceed through one particular vibration−rotation level of the electronically excited state defined by the photon energy sum. In the case of NO−Ar, the X−A spectrum is dominated by three levels defining the photon energy sums: 44242.1 (type (α)), 44272.1 (type (β)), and 44275.8 cm^{-1} (type (γ)).[38] As shown schematically in Figure 5, these levels are accessed in the hot band detection scheme. Alternatively, we used a sequence band detection scheme in which UV excitation to the corresponding levels of the A-state NO($\nu_{\mathrm{NO}}' = 2$)−Ar surface takes place.

In our experiment, the IR laser frequency is not controlled but only monitored by the computer that runs the experiment. Furthermore, the IR laser wavelength is only known approximately due to day-to-day variations in the operation of the single-mode oscillator. As a consequence, the absolute IR frequency and, thus, the resulting photon energy sum during the scan are only established after the scan has been completed by analyzing the simultaneously recorded etalon fringes and the photoacoustic spectrum of NO. In practice, we use a known IR−UV double resonance to fix the photon energy sum at the beginning of a scan. During the scan, the relative frequency of the UV laser is tracked with the relative change of the IR

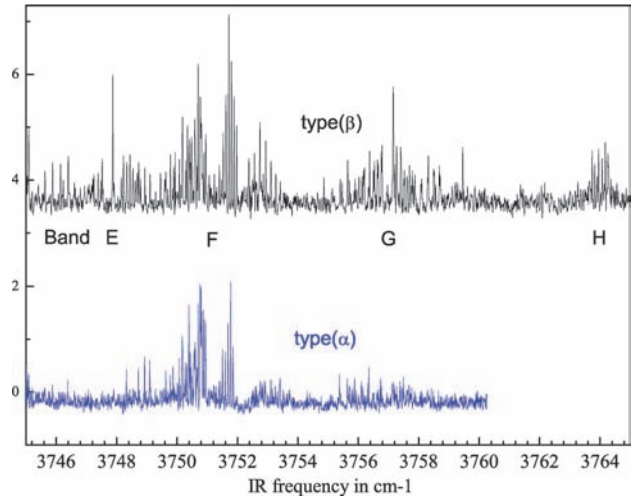

Figure 10. Comparison of constant photon energy sum scans through hot band detection types (α) and (β): first overtone and combination bands labeled E−H.

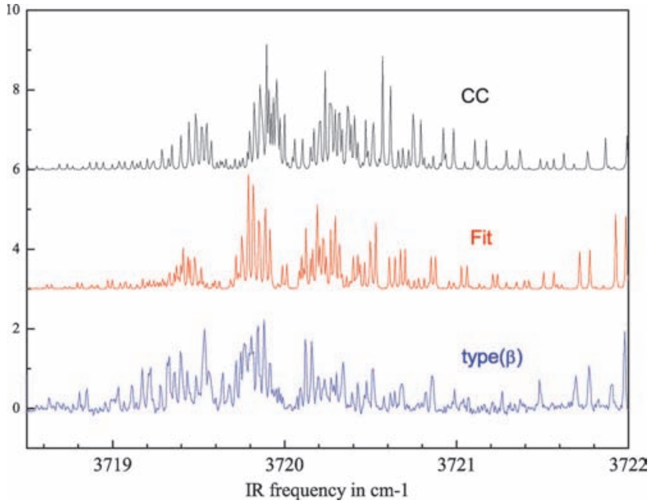

Figure 11. Comparison of calculated (CC), fitted, and experimental (type (β)) spectra; hot band $(\nu_{NO},\nu_b,\nu_s,P) = (0,0,0,1.5) \rightarrow (2,0,0,0.5)$.

frequency. Depending on the length of the scan, the photon energy sum varies within less than ±1 cm^{-1}.

In Figure 6, we present simultaneous scans of type (α) and type (β). In each scan, all major bands are observed with increased sensitivity and spectral resolution as compared to our previous experiments (see, for example, Figures 7 and 8 in ref 17). The upper panel in the figure shows the variation of the respective photon energy sum as determined after calibration of the IR frequency. Although the variation of the photon energy sum is comparable to the width of the peaks in the REMPI spectrum, it clearly exceeds the line width of the UV light, causing a nonuniform detection of the IR absorption as manifested in the abrupt intensity changes within different rotational branches.

In addition, the problem of finding the correct photon energy sum for a sequence band transition, which involves a previously unknown excited-state level, can be a challenge. We therefore try to take advantage of the fact that for many complexes, NO−X, the (1 + 1) REMPI A-state spectrum is known. This spectral information is easily exploited if, instead of sequence band detection, we employ hot band detection. Unfortunately, the required frequency is red shifted beyond the gain profile of the laser dye used for NO(ν_{NO} = 0) X−A detection. In our experiment, we resort therefore to sum frequency generation between the dye laser output and the residual second-harmonic output from the Nd:YAG pump laser.

As an additional benefit, we generate UV light with a substantially increased line width, making the detection of vibrationally excited species more uniform. From the hot band spectra of the NO monomer shown in Figure 7, we estimate the effective line width of the UV to be 2.5 cm^{-1}. Vibrationally excited NO(ν_{NO} = 2) was generated either by IR pumping on the NO Q_{11} (0.5) line or in a molecular beam discharge experiment.[39] For comparison, we also show calculated spectra (assuming a rotational temperature of 1.5 or 15 K) using the rotational constants for NO(ν_{NO} = 2) of ref 35 and those for the X−A transition from ref 36, assuming a line width of 2.5 cm^{-1}. In order to demonstrate the dramatic change in the effective line width, we superimpose on the 15 K spectrum the spectrum calculated with a line width of 0.15 cm^{-1} appropriate for the UV light generated via SHG of the dye laser output. Because the increased line width of the sum frequency UV exceeds now the variation of the photon energy sum during a simultaneous scan of the IR and UV, we expect a much more uniform detection efficiency for the IR absorption.

This is illustrated in Figures 8−10. For the NO−Ar system, all major bands, A−D, are detected for all three photon energy sum types, (α) through (γ). In comparison with our previous work, these bands are recorded with improved signal-to-noise ratio and frequency resolution. Over the frequency range covered in this study, a total of at least five additional weak bands have been measured.

Figure 8 shows the comparison of bands A and B (centered at 3723.415 and 3726.928 cm^{-1}, respectively) recorded as spectra of types (α), (β), and (γ). In the top part of this figure, we show the original spectrum recorded using fixed UV (2 + 1) REMPI hot band detection via the H state (58397.8 cm^{-1}).[17] While the overall appearance of the spectra is very similar, we notice an improvement of the spectral resolution in the constant sum scans (resolution: 0.015−0.025 cm^{-1}) compared to the measured line width (resolution: 0.036 cm^{-1}) in the original experimental setup. The improvement is attributed mainly to differences in data acquisition and OPO laser operation. In the original experiment, we monitored the ion signal with a box car integrator with exponential averaging, while in the present experiment, a fixed 8 or 16 shot averaged time-of-flight spectrum is acquired using a digital oscilloscope. Depending on the signal-to-noise level, the former method can require averaging times in excess of the minimum scan speed, causing a broadening of the lines.

A second contribution to the IR line width is attributed to the presence and amplification of transverse modes. The spectra of type (α) and type (β) were recorded using the first amplification stage of the OPO laser in a single-path configuration, while a resonator configuration was used for the spectrum recorded as type (γ). In the resonator configuration, transverse modes of the oscillator are amplified, causing the increased effective line width.

Comparing the intensity of the bands in the spectra associated with the three UV types, we find that some bands are detected with very different intensities. For example, in Figure 8, band B is much weaker in the type (α) spectrum than that in the other spectra. These variations can be attributed to differences in the Franck−Condon factors but potentially also to a propensity for UV transitions with either $\Delta P = 0$ or ±1.

In Figure 9, we present bands C and D (centered at 3738.742 and 3742.050 cm^{-1}) recorded as type (α) and type (β),

TABLE 1: Spectroscopic Constants Determined in a Linear Least-Squares Fit of the Energy Levels Obtained from the CC Calculation

band[a]	ν_b	ν_s	P	$E_{\nu P}$	$B_{\nu P1}$	$B_{\nu P0}$	V_{20}	V_{21}	C_{20}	C_{21}
A	0	0	0.5	0.057	0.0070	0.0677	0.0840	0.0175	0.0096	0.0032
B	0	0	1.5	3.674	0.0089	0.0678	0.2105	0.0001	0.0004	−0.0003
B1	0	0	2.5	10.798	0.0080	0.0670	0.2740	0.0000	0.0000	0.0000
C	1	0	0.5	14.329	0.0029	0.0625	0.5761	0.0035	0.0013	0.0005
D1	1	0	1.5	20.545	0.0991	0.0605	0.3218	0.0148	0.0113	−0.0148
E	1	0	2.5	30.470	0.0131	0.0651	0.4330	0.0009	0.0004	0.0001
D	0	1	0.5	19.843	−0.0336	0.0548	0.1485	0.0452	0.1141	−0.0072
na	0	1	1.5	27.087	0.0170	0.0582	0.4276	0.0196	0.0088	−0.0061
na	0	1	2.5	36.738	−0.2063	0.0908	0.2955	0.2437	0.0017	−0.0005
F	2	0	0.5	27.122	0.0260	0.0549	0.6878	0.0128	0.0004	0.0092
na	2	0	1.5	36.827	0.0293	0.0553	1.0470	0.0027	0.0045	−0.0020
G	1	1	0.5	33.479	0.0154	0.0611	1.1083	0.0045	0.0005	0.0014
na	1	1	1.5	42.176	−0.0020	0.0617	1.2069	0.0252	0.0016	−0.0026
H	0	2	0.5	39.509	0.0104	0.0552	0.1657	0.0589	0.1220	0.0148

[a] The band labels refer to Figure 12.

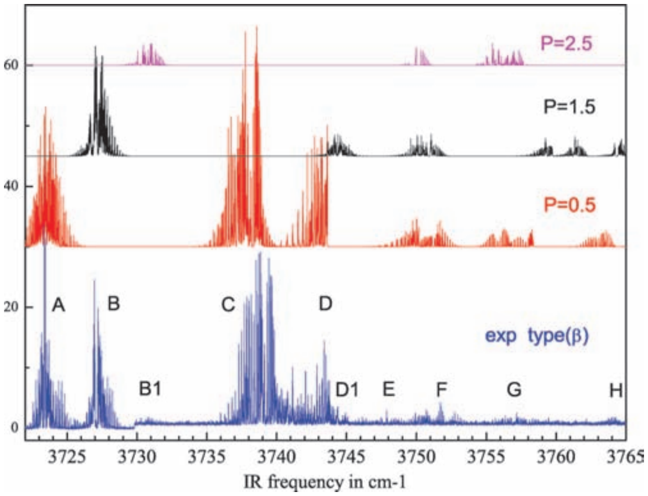

Figure 12. Spectra generated from the results of the CC calculation. The spectra are labeled by the nominal value of the quantum number P in the final state. Note that final states with $P = 2.5$ are accessed only as hot band transitions originating from the lowest excited level with $P = 1.5$.

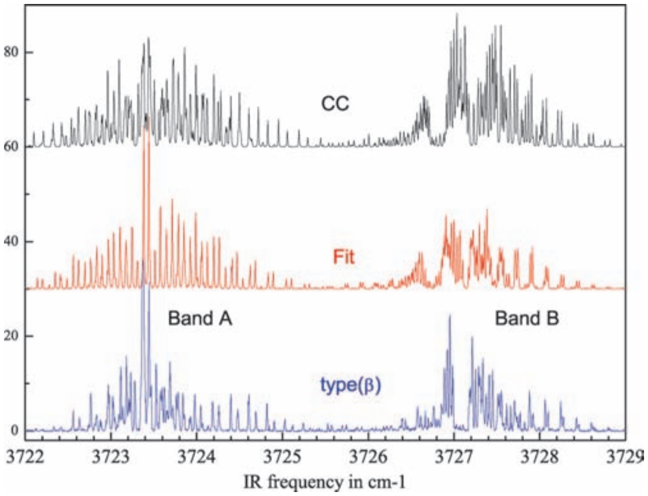

Figure 13. Comparison of calculated (CC), fitted, and experimental (type (β)) spectra: Bands A and B.

respectively. The more uniform IR detection due to the increased UV line width results in a smooth intensity variation within particular rotational branches. We also note that in the type (β) spectrum, many more lines appear at around 3741 cm^{-1}.

TABLE 2: Spectroscopic Constants Determined in a Fit to the Experimental Spectrum[a]

band	ν_b	ν_s	P	$E_{\nu P}$	$B_{\nu P0}$	V_{20}	V_{21}	C_{20}
A	0	0	0.5	0.000	0.0680	0.0440	0.0365	0.0145
B	0	0	1.5	3.513	0.0683	0.1569	0.0000	0.0000
B1	0	0	2.5	10.565	0.0681	na	na	0.0000
C	1	0	0.5	15.327	0.0632	0.4653	0.0000	0.0123
D1	1	0	1.5	20.804	0.0738	0.7144	0.0000	0.0145
E	1	0	2.5	28.185	0.0653	na	na	0.0000
D	0	1	0.5	18.635	0.0681	0.7760	0.0000	0.0140
F	2	0	0.5	27.770	0.0691	0.8999	0.0000	0.0138
G	1	1	0.5	34.538	0.0625	1.0621	0.0000	0.0098
H	0	2	0.5	40.145	0.0665	0.0644	0.0000	0.0145
HB	0*	0*	1.5	3.590	0.0680	0.1999	0.0000	0.0000

[a] Because only one ω component could be identified for bands B1 and E, no splitting constants V_{20} and V_{21} were determined for these bands. The quantum numbers marked with an asterisk indicate the entries determined from the observed hot band, that is, they refer to the NO($\nu_{NO} = 0$)−Ar surface.

An important advantage of the present method concerns the detection of unknown weak bands. Because the constant photon energy sum ensures the resonance condition for the UV excitation step as long as the IR laser hits a resonance, weak bands are detected if the associated transition dipole matrix element including the Franck−Condon factor are large enough to yield signals above the noise level. Even at higher IR frequencies very weak bands due to overtones and combination bands of the intermolecular vibrations are detected. In Figure 10, we present spectra recorded as type (α) and type (β) in the frequency range up to 3765 cm $^{-1}$.

Finally, we employ the increased sensitivity of the present experiment to search for hot band transitions. For these experiments, the UV frequency is kept fixed to excite the A-state levels α, β, or γ while the IR frequency is scanned. One hot band is found shifted 3.5 cm^{-1} to the red of band A. It is attributed to a transition from the vibrationless level with $P'' = 1.5$ of the NO($\nu_{NO} = 0$)−Ar surface to the ground-state level of the NO($\nu_{NO} = 2$)−Ar surface. In Figure 11, we compare the experimental type (β) spectrum with the spectrum based on the CC calculation for NO−Ar($\nu_{NO} = 0$) and the fit to the experiment. Apart from a small frequency shift on the order of 0.1 cm^{-1}, the calculated band shows almost the same rotational structures as the experimental spectrum.

5. Spectroscopic Analysis and Discussion

Guided by the results from the exact close-coupling bound-state calculations, we were able to represent the NO−Ar

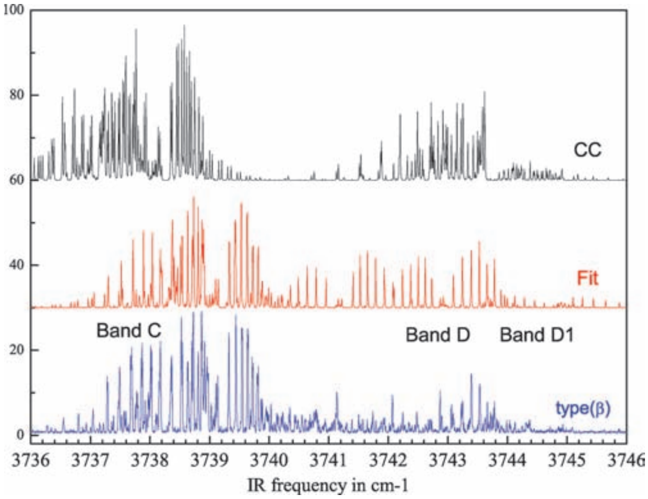

Figure 14. Comparison of calculated (CC), fitted, and experimental (type (β)) spectra: Bands C and D.

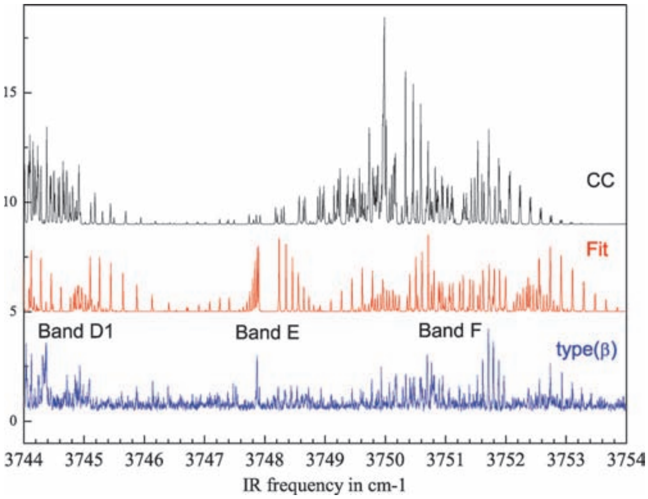

Figure 15. Comparison of calculated (CC), fitted and experimental (type (β)) spectra: Bands E and F.

rovibrational energy levels by an analytical expression involving a small set of spectroscopic constants.[11] Under the assumption of a nearly T-shaped structure for the complex and if the NO−Ar interaction potential is neglected, the rotational levels have the structure of those for a symmetric top with a 4-fold degeneracy due to the projections of the NO electronic angular momentum ω ($\omega = \pm 1/2$ and 3/2) onto the internuclear axis of the diatom and the projections $\pm P$ of the total angular momentum onto the body-frame z-axis. The degeneracies are lifted by V_{sum} (the average interaction potential), which gives rise to a splitting into two near-degenerate levels characterized by the sign of the product $P\omega$. In recognition of this fact, the associated spectroscopic constants will be distinguished by ± subscripts.

The remaining degeneracy is lifted by V_{diff} (the difference potential). This term (V_{diff}) couples states with $\Delta P = \pm 1$ and therefore splits each remaining pair of degenerate $P\omega$ levels into two levels characterized by a symmetry quantum number $\eta = \pm 1$ which is related to the overall parity of the state. We refer to this effect as P-type doubling.[40]

Quantitatively, we can express the energies in the following form

$$E_{\nu JP\omega\eta} = E_{\nu P} + B_{\nu P0}J(J+1) + B_{\nu P1}\left(J+\frac{1}{2}\right) + \sum_{n=0}^{2}\left(\eta F_{2n} + \frac{\omega}{|\omega|}V_{2n} + \eta\frac{\omega}{|\omega|}C_{2n}\right)\left(J+\frac{1}{2}\right)^{n} \quad (1)$$

For consistency, we have written the expression in terms of a P-type doubling contribution (η splitting), which is independent of ω (with coefficients F_{2n}), and one which is ω-dependent (with coefficients C_{2n}). We also included a term for the average energy, which is linear in (J + 1/2).

As Hutson and co-workers have pointed out,[41] the ω splitting can be expected to be very small for a near-linear complex. However, depending on the strength of the interaction, for a T-shaped complex, this splitting might be greater than the rotational level spacing. In the latter case, it is more convenient to define separate ω bands with individual rotational and P-type doubling structures. Accordingly, we rearrange the above expression into the following form

$$E_{\nu JP\omega\eta} = E_{\nu P\omega} + B_{\omega}J(J+1) + V_{\omega}\left(J+\frac{1}{2}\right) + \eta\sum_{n=0}^{2}\frac{1}{2}d_{2n}^{\omega}\left(J+\frac{1}{2}\right)^{n} \quad (2)$$

Rearranging the equations and sorting out the different terms, the spectroscopic constants are easily converted between the models, namely

$$E_{\nu P} = \frac{E_{\nu P+} + E_{\nu P-}}{2} \qquad B_{\nu P0} = \frac{B_{+} + B_{-}}{2}$$
$$B_{\nu P1} = \frac{V_{+} + V_{-}}{2} \qquad V_{20} = \frac{E_{\nu P+} - E_{\nu P-}}{2} - \frac{B_{+} - B_{-}}{8}$$
$$V_{21} = \frac{V_{+} - V_{-}}{2} \qquad V_{22} = \frac{B_{+} - B_{-}}{2}$$
$$F_{2n} = \frac{d_{2n}^{+} + d_{2n}^{-}}{4} \qquad C_{2n} = \frac{d_{2n}^{+} - d_{2n}^{-}}{4} \quad (3)$$

We assign a nominal value of the projection quantum number P to each bend−stretch state determined in the exact CC calculations by comparing its energy to the results of comparable bound-state calculations within the CS approximation, where P is a good quantum number. Unfortunately, in the case of nearly degenerate levels, this procedure can be ambiguous. Notwithstanding, we used a linear least-squares procedure to fit the calculated CC level positions by the spectroscopic parameters defined in eq 1. We included all rotational levels up to $J = 4.5$. The resulting constants are listed in Table 1. For $P = 0.5$, 1.5, and 2.5, 20, 16, or 12 levels, respectively, were used to the fit the 12 spectroscopic constants.

In practice, several of the constants turn out to be negligibly small. For example, we could restrict the terms describing the η splitting to linear powers in $J + 0.5$, that is, $C_{22} = 0$, while the η splitting of the ω-averaged energy can be neglected, (that is, $F_{2n} = 0$). Even for the averaged energy, the term linear in J is very small for most bands. Taking these restrictions into account, we find that the energy of most states is well described by the vibrational energy $E_{\nu P}$, the rotational constant $B_{\nu P0}$, the electrostatic splitting V_{20}, and the P-type doubling constant C_{20}. Quantitatively, the calculated energies are reproduced by the fit to within 0.005 cm^{-1}, which is clearly well below the effective resolution of the experiment, or, for that matter, well within the precision of the bound-state calculations.

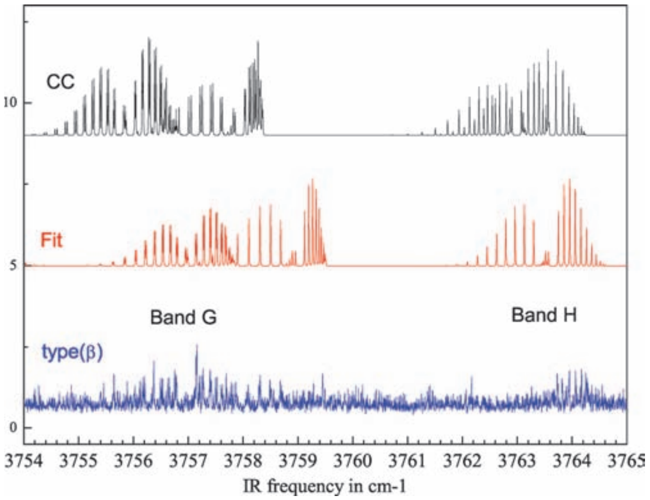

Figure 16. Comparison of calculated (CC), fitted, and experimental (type (β)) spectra: Bands G and H.

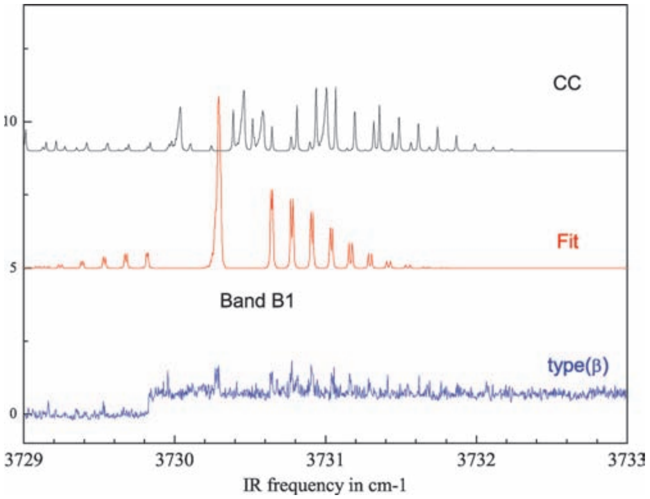

Figure 17. Comparison of calculated (CC), fitted, and experimental (type (β)) spectra: Band B1 (hot band $(\nu_{NO},\nu_b,\nu_s,P) = (0,0,0,1.5) \rightarrow (2,0,0,2.5)$).

Although the near-IR spectrum involves transitions between bound levels of the NO($\nu_{NO} = 0$)−Ar surface to levels of the NO($\nu_{NO} = 2$)−Ar potential, we neglect any dependence of the spectroscopic constants in Table 1 on the NO vibrational quantum number. This assumption is supported by the very small red shift of 0.44 cm^{-1} of the origin of the near-IR spectrum of NO−Ar with respect to the corresponding monomer transition. It is also consistent with the set of spectroscopic constants experimentally determined for the first excited level with $P = 1.5$ of the NO($\nu_{NO} = 0$)−Ar and of the NO($\nu_{NO} = 2$)−Ar surfaces obtained from the analysis of the hot band $(\nu_{NO},\nu_b,\nu_s,P)=(0,0,0,1.5) \rightarrow (2,0,0,0.5)$ and band B, respectively. For these particular levels, the experimental constants derived for both surfaces are indeed very similar.

On the other hand, the mere fact that bands associated with the excitation of intermolecular vibrations are observed could, in principle, indicate important differences in the wave functions preventing the overlap integrals from completely vanishing. Along this line of thought, we would expect the overtone transitions to have a comparable or even larger intensity than that of the fundamentals because of the better match in symmetry. In the experiment, we find the overtone and combination bands to be much weaker than the fundamentals. This intensity pattern is thus very similar to the case of a typical molecular vibration where the dominant intensity of the fundamental is due to the slope (first derivative) of the transition dipole moment function, while its curvature (second and higher derivatives) contributes to the intensity of the much weaker overtones. Therefore, we interpret the relative intensities of the observed bands in terms of a small dependence of the transition dipole moment function on the intermolecular coordinates in addition to its dependence on the NO internuclear distance.

With these limitations in mind, we generate a theoretical near-IR spectrum by shifting the energy differences between the levels found in the CC calculation by the frequency corresponding to the center of the origin band, 3723.415 cm^{-1}. As described in ref 11, we calculate an approximate line strength based on the adiabatic-bender approximation. Both parallel and perpendicular components of the transition moment vector are included with their ratio kept as an adjustable parameter. Finally, the overall intensity of a band is adjusted empirically through a Franck−Condon factor assuming a Boltzmann distribution with a temperature of ~1.5 K. Using the parameters fitted to the results of the CC calculation, we generate the spectra displayed in Figure 12 for transitions from levels with $P'' = 0.5$ to levels with $P' = 0.5$ and 1.5. We also show the calculated spectrum for the hot band transitions from ground-state levels with $P'' = 1.5$ to excited-state levels with $P' = 2.5$. Note that the intensities for the individual bands of the calculated spectra are adjusted empirically to roughly match the experimental ones, or in the case of no experimental counterpart, they are given some minimum intensity in order to indicate their position in Figure 12.

***P*-Type Structure.** As in the experiment, the calculated spectrum is extremely rich. At least nine bands can be identified, which we label A−H. Because each band extends over several wavenumbers, some bands overlap even at the low temperature of our molecular beam. Nevertheless, the calculated spectrum reproduces the position and rotational structure of most bands very well. According to the theoretical treatment, the main bands are due to transitions between levels with $P = 0.5$, that is $\Delta P = 0$. Of the transitions to levels with $P' = 1.5$, that is, $\Delta P = +1$, only band B has significant intensity. Comparing the observed intensities of bands with $P' = 0.5$ and 1.5, we find that the former clearly dominate. This preference is especially obvious in the spectra recorded as type (α). Because the weak bands recorded in the range from 3750 to 3765 cm^{-1} are present in the type (α) as well as the type (β) spectra, we assign them to the first overtone of the bending and stretch vibrations and their combination band with $P' = 0.5$. On the other hand, bands B1 and E are only observed in the type (β) spectrum and are thus assigned to involve hot band transitions to levels with $P' = 2.5$.

An inspection of Table 1, shows that the excitation energy between different P levels increases significantly for the vibrationally excited states as compared to that for the vibrationless ground levels. Approximating the P dependence of the rotational energy by just the symmetric top term $E_{rotP} = bP^2$, we deduce from the observed energy spacing between the $P = 0.5$ and 1.5 levels of the vibrationless ground state that $b \approx B_{NO}$, as expected for a T-shaped complex. For the vibrationally excited levels, the spacing almost doubles for the fundamental and more than doubles for the overtones. These changes indicate a significant deviation of the vibrationally averaged structure from the T-shaped configuration. Note that in the limit of a linear structure, the associated energy spacing diverges.

Vibrational Structure. In order to permit a quantitative comparison of the band positions, we adjust the spectroscopic constants defined in eq 2 to get the best fit to the experimental spectrum. Guided by the results of the fit to the CC-calculated level positions, we include only the constants $E_{\nu P}$, $B_{\nu P0}$, V_{20}, V_{21}, and C_{20} (all other constants in eq 2 were set to zero). This defines a minimum set of adjustable parameters. The resulting constants are converted to the ones defined in eq 1 and summarized in Table 2. The calculated "best fit" spectrum is compared with the results of the CC calculation and the experimental spectrum of type (β) in Figures 11 and 13–17. The comparison of the bend–stretch energies ($E_{\nu P}$) in both tables demonstrates the great accuracy of the CC calculation. The calculated energies are predicted accurately within at least 2 cm^{-1}; for many levels, the agreement is better than 1 cm^{-1}. The fundamental bending and stretch frequencies are 14.3 and 19.8 cm^{-1} for the CC calculation, while the best fit yields 15.3 and 18.6 cm^{-1}, respectively. Interestingly, the associated first overtone levels agree within 0.6 cm^{-1}, while the first combination band is reproduced to within 1 cm^{-1}. To a first approximation, for a given value of P, the intermolecular vibrational motion of NO–Ar can be represented well as two independent harmonic oscillators in the bending and stretching motion with only a small anharmonicity.

Rotational Structure. As discussed above, the fine structure of the observed bands is due to the variation of the rotational energy, the electrostatic ω splitting, and the P-type doubling. Although a complicated structure can be expected, many of the observed bands show several rotational branches with a smooth intensity variation. While it was not possible to fit the spectra using the originally developed form of the empirical Hamiltonian (see eq 1), a much more satisfactory fit with a minimum number of adjustable parameters could be obtained using the energy expression given in eq 2. In this form, individual branches can be identified as belonging to a particular ω component of the band. On the other hand, the following discussion is facilitated by considering the energy levels to be split as a result of the average or difference potentials. Therefore, Tables 1 and 2 list the constants as defined according to eq 1.

Apart from the small overall shifts in the band positions discussed above, we find fitted rotational structures very similar to the results based on the CC calculations. The rotational constants for bands A, B, B1, C, E, G, and the hot band are found to agree within 0.001 cm^{-1}. For the vibrationless ground level and the pure stretch levels, the ω splitting due to the average potential does not exceed 0.2 cm^{-1}. In contrast, it increases significantly with excitation of P-rotation and bending vibrations reaching values of about 1 cm^{-1}. These trends are well reflected in the result of the calculation. Furthermore, for most levels, the splitting agrees within 0.1 cm^{-1}. Note that for bands E and B1, constants V_{2n} were not determined because only one ω component was identified experimentally.

For the other bands, notably D and F, a direct comparison of the rotational constants is difficult because in the fit to the CC results, the linear coefficient $B_{\nu P1}$ cannot be neglected. We attribute this anomalous behavior to the presence of a perturbation. In this context, it is interesting to note that the energies for these levels are nearly degenerate with levels $(\nu_{NO},\nu_b,\nu_s,P) = (0,1,0,1.5)$ and $(0,0,1,1.5)$, respectively. Because the pairs of degenerate levels belong to different P values, a possible mixing requires the breakdown of the adiabatic-bender approximation. Coriolis coupling terms involve the shift operators for the body-fixed representation of the total angular momentum vector components and will therefore mix basis states with different P.

In our previous work, we have shown that the P-type doubling can be explained through the coupling of basis states with $P = \pm 0.5$ via the difference potential.[11] Because no direct coupling of states with $P = \pm 1.5$ through the difference potential is possible, the P-type doubling of levels with $|P| = 1.5$ or 2.5 involves higher-order Coriolis couplings. It is for this reason that these levels effectively have no P-type doubling, that is, $C_{2n} = 0$. This is indeed found in both the experimental and the theoretical results, except for the perturbed levels $(\nu_{NO},\nu_b,\nu_s,P) = (\nu_{NO},1,0,1.5)$, and $(\nu_{NO},0,1,1.5)$.

The difference between experiment and theory is especially significant for the first stretch level, that is, for band D. Because of the strongly reduced rotational constant in combination with a negative linear rotational energy contribution, the theoretical band is dominated by a band head near 3743.5 cm^{-1}, which is not observed in the experimental spectrum at all. For example, the best fit yields for the excited state accessed in band D a rotational constant $B_{\nu P0}$ almost identical to that of the ground level. This causes the band to be much more evenly spread out than predicted by the spectral simulation based on the CC calculations. The situation for band F is not as bad because the linear rotational energy contribution is positive here, giving rise to a rotational structure similar to the experimentally observed one.

Bands B1 and E are hot band transitions $(\nu_{NO},\nu_b,\nu_s,P) = (0,0,0,1.5) \rightarrow (2,0,0,2.5)$ and $(0,0,0,1.5) \rightarrow (2,1,0,2.5)$, respectively. While the rotational constants predicted in the CC calculation agree very well with the experimental best fit, both bands are predicted to show a considerable ω splitting, which is not observed experimentally. Due to this splitting, we find many more lines in the calculated spectrum. Also, the predicted positions of both bands are shifted toward higher energy. As we discussed above, small deviations from the T-shaped structure can cause a large increase in the P-level energy spacings. As a result of a shift of 2 cm^{-1} toward higher wavenumbers, in the theoretical spectrum, band E overlaps completely with band F. The latter thus appears more complex in the region of 3750 cm^{-1}. With this realization, we find that, apart from the shift in the band center, the predicted rotational structure for band F does agree well with the experimental spectrum.

6. Conclusion

The near-IR spectrum of the NO–Ar complex has been measured with greatly increased sensitivity by employing constant photon energy sum scans as a new variant of IR-REMPI double spectroscopy. Combined with broadband UV hot band detection, the method ensures the optimum IR absorption detection efficiency, as can be expected in a double resonance scheme. For the NO–Ar complex, the method enables us to detect for the first time very weak bands assigned to the overtone and combination bands of the intermolecular vibrations or hot bands.

The spectra are assigned with the help of results from a full CC bound-state calculation. For the quantitative comparison between experiment and theory, we represent the calculated energy levels in terms of a set of spectroscopic constants defining an empirical model Hamiltonian. Through variation of these constants, and guided in their initial choice by the fit to the CC calculations, we obtain a set of parameters which provide a best fit to the experimental spectrum. For most observed bands, we find excellent agreement between theory and experiment.

More significant deviations occur for the fundamental stretch vibration. The CC calculation predicts a significantly lower rotational constant than that observed in the experiment. Most likely, the cause is the interaction with a nearly degenerate second vibrational level due to Coriolis coupling. For the other bands, vibrational energies, rotational, ω splitting, and P-type doubling constants are predicted with only minimal discrepancies, demonstrating the overall accuracy of the ab initio PESs. The slight remaining discrepancies are likely a measure of the incomplete recovery of the correlation energy in the CCSD(T) calculations of Alexander.[15]

Another possible origin of the small differences seen here is that in these ab initio calculations, the NO molecule was held fixed at its equilibrium internuclear distance. We might expect a small difference between the NO($v = 2$)−Ar and NO($r = r_e$)−Ar PESs. As we have seen, the fit to experiment of the constants for the hot band and band B differ by an amount comparable to the differences in the constants arising from the fit to experiment and the fit to the calculated spectra. Quite possibly, the discrepancies could be reduced by determining the NO−Ar PESs at a number of values of the NO bond distance and then averaging over the NO($v = 2$) vibrational wave function.

Notwithstanding, the overall good agreement seen here between the results of the CC calculations and the fit to experiment, as well as the good agreement seen in the simulations of recent scattering experiments,[9,10] indicates that the PESs of Alexander[15] provide an accurate description of the NO−Ar interaction.

Acknowledgment. J.K. and M.H.A. are grateful to the U.S. National Science Foundation for financial support under Grant No. CHE-0413743. B.W., Y.K., and H.M. gratefully acknowledge the financial support provided by the National Science Foundation under Grant No. CHE-0097189.

References and Notes

(1) Nesbitt, D. J. *Annu. Rev. Phys. Chem.* **1994**, *45*, 367.
(2) Bacic, Z.; Miller, R. E. *J. Phys. Chem.* **1996**, *100*, 12945.
(3) See the issue “Van der Waals III” *Chem. Rev.* **2000**, *100*, issue 11.
(4) Carter, C. C.; Lee, H. S.; McCoy, A. B.; Miller, T. A. *J. Mol. Struct.* **2000**, *525*, 1.
(5) Heaven, M. C. *Int. Rev. Phys. Chem.* **2005**, *24*, 375.
(6) Thuis, H.; Stolte, S.; Reuss, J. *Chem. Phys.* **1979**, *43*, 351.
(7) Thuis, H.; Stolte, S.; Reuss, J.; van den Biesen, J. J. H.; van den Meijdenberg, C. J. N. *Chem. Phys.* **1980**, *52*, 211.
(8) Gijsbertson, A.; de Lange, M. J. L.; Wiskerke, A. E.; Linnartz, H.; Drabbels, M.; Klos, J.; Stolte, S. *Chem. Phys.* **2004**, *301*, 293.
(9) Lorenz, K. T.; Chandler, D. W.; Barr, J. W.; Chen, W.; Barnes, G. L.; Cline, J. I. *Science* **2001**, *293*, 2063.
(10) Kohguchi, H.; Suzuki, T.; Alexander, M. H. *Science* **2001**, *294*, 832.
(11) Kim, Y.; Meyer, H. *Int. Rev. Phys. Chem.* **2001**, *20*, 219.
(12) Mills, P. D. A.; Western, C. M.; Howard, B. J. *J. Phys. Chem.* **1986**, *90*, 3331.
(13) Mills, P. D. A.; Western, C. M.; Howard, B. J. *J. Phys. Chem.* **1986**, *90*, 4961.
(14) Sumiyoshi, Y.; Endo, Y. *J. Chem. Phys.* **2007**, *127*, 184309.
(15) Alexander, M. H. *J. Chem. Phys.* **1999**, *111*, 7426.
(16) Alexander, M. H. *J. Chem. Phys.* **1999**, *111*, 7435.
(17) Kim, Y.; Fleniken, J.; Meyer, H.; Alexander, M. H.; Dagdigian, P. J. *J. Chem. Phys.* **2000**, *113*, 73.
(18) Kim, Y.; Fleniken, J.; Meyer, H. *J. Chem. Phys.* **2001**, *114*, 5577.
(19) Akiike, M.; Tsuji, K.; Shibuya, K.; Obi, K. *Chem. Phys. Lett.* **1995**, *243*, 89.
(20) Mack, P.; Dyke, J. M.; Smith, D. M.; Wirght, T. G. *Chem. Phys. Lett.* **1997**, *284*, 423.
(21) Daire, S. E.; Lozeille, J.; Gamblin, S. D.; Lee, E. P.; Wright, T. G. *Chem. Phys. Lett.* **2001**, *346*, 305.
(22) Utz, A. L.; Carrasquillo, M., E.; Tobiason, J. D.; Crim, F. F. *Chem. Phys.* **1995**, *190*, 311.
(23) Milce, A. P.; Orr, B. J. *J. Chem. Phys.* **1996**, *104*, 6423.
(24) Kim, Y.; Patton, K.; Fleniken, J.; Meyer, H. *Chem. Phys. Lett.* **2000**, *318*, 522.
(25) HIBRIDON, is a package of programs for the time-independent quantum treatment of inelastic collisions and photodissociation written by Alexander, M. H.; Manolopoulos, D. E.; Werner, H -J.; Follmeg, B. with contributions by Vohralik, P. F.; Lemoine, D.; Corey, G.; Gordon, R.; Johnson, B.; Orlikowski, T.; Berning, A.; Degli-Esposti, A.; Rist, C.; Dagdigian, P.; Pouilly, B.; van der Sanden, G.; Yang, M.; de Weerd, F.; Gregurick, S.; Kłos, J. More information is available on the website http://www.chem.umd.edu/groups/alexander/hibridon/hib43.
(26) (a) Alexander, M. H. *J. Chem. Phys.* **1982**, *76*, 5974. (b) Alexander, M. H. *Chem. Phys.* **1985**, *92*, 337.
(27) Hamilton, I. P.; Light, J. C. *J. Chem. Phys.* **1986**, *84*, 306.
(28) Holmgren, S. L.; Waldman, W.; Klemperer, W. *J. Chem. Phys.* **1977**, *67*, 4414.
(29) Alexander, M. H.; Gregurick, S.; Dagdigian, P. J. *J. Chem. Phys.* **1994**, *101*, 2887.
(30) Kouri D. J. In *Atom−Molecule Collision Theory: A Guide for the Experimentalist*; Bernstein R. B., Eds.; Plenum: New York, 1979; p 301.
(31) Meyer, H. *J. Chem. Phys.* **1994**, *101*, 6686.
(32) Meyer, H. *J. Chem. Phys.* **1994**, *101*, 6697.
(33) Kim, Y.; Ansari, S.; Zwickel, B.; Meyer, H. *Rev. Sci. Instrum.* **2003**, *74*, 4805.
(34) (a) Bosenberg, W. R.; Guyer, D. R. *J. Opt. Soc. Am. B* **1993**, *10*, 1716. (b) Bosenberg, W. R.; Guyer, D. R. *Appl. Phys. Lett.* **1992**, *61*, 387.
(35) Amiot, C.; Bacis, R.; Guelachvili, G. *Can. J. Phys.* **1978**, *56*, 251.
(36) Miescher, E.; Huber, K. P. In *Int. Rev. Sci., Phys. Chem. Ser. 2*; Buckingham A. D., Ramsay, D. A., Eds.; Butterworths: London, 1973; Vol. 3, p 37.
(37) Nikogosyan, D. N. *Appl. Phys. A* **1991**, *52*, 359.
(38) Lozeille, J.; Gamblin, S. D.; Daire, S. E.; Wright, T. G. *J. Chem. Phys.* **2000**, *213*, 7224.
(39) Fleniken, J.; Kim, Y.; Meyer, H. *Chem. Phys. Lett.* **2000**, *318*, 529.
(40) Dubernet, M. L.; Tuckey, P. A.; Hutson, J. M. *Chem. Phys. Lett.* **1992**, *193*, 355.
(41) Dubernet, M. L.; Flower, D.; Hutson, J. M. *J. Chem. Phys.* **1991**, *94*, 7602.

JP802765Z